



저작자표시-비영리-변경금지 2.0 대한민국

이용자는 아래의 조건을 따르는 경우에 한하여 자유롭게

- 이 저작물을 복제, 배포, 전송, 전시, 공연 및 방송할 수 있습니다.

다음과 같은 조건을 따라야 합니다:



저작자표시. 귀하는 원저작자를 표시하여야 합니다.



비영리. 귀하는 이 저작물을 영리 목적으로 이용할 수 없습니다.



변경금지. 귀하는 이 저작물을 개작, 변형 또는 가공할 수 없습니다.

- 귀하는, 이 저작물의 재이용이나 배포의 경우, 이 저작물에 적용된 이용허락조건을 명확하게 나타내어야 합니다.
- 저작권자로부터 별도의 허가를 받으면 이러한 조건들은 적용되지 않습니다.

저작권법에 따른 이용자의 권리는 위의 내용에 의하여 영향을 받지 않습니다.

이것은 [이용허락규약\(Legal Code\)](#)을 이해하기 쉽게 요약한 것입니다.

[Disclaimer](#)

Master's Thesis of Engineering

**Stereovision-based Ridge-Furrow
Detection and Tracking System for
Autonomous Seeding**

자율파종을 위한 두둑검출 및 추종시스템

February 2020

**Graduate School of Agriculture and Life Sciences
Seoul National University
Major of Biosystems Engineering**

CHANGHO YUN

Stereovision-based Ridge-Furrow Detection and Tracking System for Autonomous Seeding

Professor HAK-JIN KIM

Submitting a master's thesis of Engineering

February 2020

**Graduate School of Agriculture and Life
Sciences
Seoul National University
Major of Biosystems Engineering**

CHANGHO YUN

**Confirming the master's thesis written by
CHANGHO YUN
February 2020**

Chair Joong-Yong Rhee (Seal)

Vice Chair Hak-Jin Kim (Seal)

Examiner Ghi-Seok Kim (Seal)

Abstract

This paper proposes a stereovision-based auto-guidance method for a riding cultivator. Ridge and furrow are corrugated field structures created before seeding operation for good water balance in a field. The stereovision provides the ability to aware these field structures and determine a navigation path. In developing an efficient ridge and furrow classification algorithm for the outdoor application, however, the stereovision would suffer from the erratic movement of a vehicle on uneven surface and interferences caused by strong sunlight. The developed algorithm adopts a combination of v-disparity representation, the Otsu's thresholding and a roll angle compensation method proposed to overcome the problems. Feasibility tests were conducted using video data collected under outdoor conditions to analyze the image classification accuracy of the algorithm. The developed algorithm was able to classify the ridge and furrow with over 90% of accuracy in the rough outdoor conditions. Field testing with the automatic guided riding cultivator equipped with the stereo camera proved the developed ridge tracking algorithm would be applicable to a real-world agricultural application, showing the lateral deviations of the average RMSE of 2.5cm and 6.2cm in a flat field and a hilly field respectively.

Keyword : Stereo camera, ridge/furrow, riding cultivator, potato seeding, auto-guidance

Student Number : 2017-23806

Table of Contents

Chapter 1. Introduction	1
1.1. Study Background	1
1.2. Purpose of Research	2
1.3. Review of Literature	3
Chapter 2. Materials and Methods	6
2.1. Ridge and Furrow.....	6
2.2. Principle of Stereovision	8
2.3. Ridge and Furrow Detection and Tracking Algorithm	11
2.3.1 Ridge and Furrow Classification Algorithm using v-	
disparity and Otsu's thresholding	12
2.3.2 Roll Angle Compensation	15
2.3.3 Sliding Window Technique.....	17
2.3.4 ROI Setting	18
2.3.5 Path Tracking Model	19
2.4. Feasibility Tests.....	23
2.4.1 Data Collection.....	23
2.4.2 Image Classification Accuracy Analysis.....	25
2.5. Field Testing	26
2.5.1 Ridge Tracking System	26
2.5.2 Test Fields and Performance Evaluation	28

Chapter 3. Results and Discussion	31
3.1. Effect of Sunlight on Detection Performance	31
3.2. Feasibility of Using Roll Angle Compensation Method for Uneven Surface Movement	33
3.3. Field Test Result.....	35
 Chapter 4. Conclusions	 38
 Bibliography	 39
 Abstract in Korean	 43

Tables

Table 1 Result for the daylight feasibility test.....	31
Table 2 Result for the dynamic situation feasibility test	34
Table 3 RMSE of the ridge tracking result.....	37

Figures

Fig. 1 Corrugation, ridge and furrow	6
Fig. 2 Dimension of the 15kW riding cultivator developed by TYM	7
Fig. 3 Stereovision (“Image rectification”, 2019)	8
Fig. 4 Rectification (“Image rectification”, 2019)	9
Fig. 5 Ridge-furrow detection and tracking algorithm	11
Fig. 6 (a) Left image (b) Right image (c) v-disparity image	12
Fig. 7 Ridge and furrow classification using v-disparity map and Otsu’s method (a) A row in v-disparity map (b) Disparity image (c) v-disparity map	14
Fig. 8 (a) Color image (b) Binary image of ridge and furrow ...	14
Fig. 9 Image projection problem caused by a rolling offset	15
Fig. 10 (a) Plot of disparity isolines in image coordinate (b) Geometric relationship between the isolines and rolling offset ..	16
Fig. 11 Guidance line extraction using sliding window method .	17
Fig. 12 (a) Region of Interest, ROI (b) Disparity image without occlusion filling (c) Disparity image after applying occlusion filling.....	18
Fig. 13 Guidance line schematic (a) projected field view (b) Components on the image	20

Fig. 14 Geometric relations between the camera, the vehicle and the surface (a) side view (b) 3D view	22
Fig. 15 Image collecting environment (a) Camera installation (b) Google Earth view of the test field (c) Illuminance during day hours	24
Fig. 16 Stereovision based ridge tracking system overview ...	27
Fig. 17 Size of ridge.....	28
Fig. 18 A and B points on the ridge.....	29
Fig. 19 A and B points in the UTM coordinate	30
Fig. 20 GPS point data gap	30
Fig. 21 Feasibility test result under daylight condition.....	31
Fig. 22 Errors caused by sunlight.....	32
Fig. 23 Feasibility test result under condition of vehicle moving on uneven surface.....	34
Fig. 24 An example of erratic result of guidance line extraction (a) without rolling offset compensation (b) with rolling offset compensation	34
Fig. 25 Lateral devotion between auto-guided path and manually-driven path on (a) flat field (b) hilly field.....	35
Fig. 26 Trajectory plot (a) flat field (b) hilly field	36
Fig. 27 Steering angle command (a) flat field (b) hilly field	37

Chapter 1. Introduction

1.1. Study Background

During the manual operation of a farm machine in a field, an operator controls its steering by referring to field objects such as crop row, windrow, ridge and furrow. Previous studies have focused on vision applications for crop presented season operations because the distinguish color difference between soil and crop was a readily identifiable feature to guide the machine. For farm operations before crop exists, however, the traditional crop row detection methods are not applicable due to the lack of the color characteristic. Ridge and furrow are undulating and corrugated microtopography created for irrigation and drainage, especially for row crops. Due to the three-dimensional characteristic of ridge and furrow, the operator could easily distinguish the traversable path during a seeding or planting. The interest in implementation of 3D imaging to agriculture has also been on the rise as the 3D camera technology has become more accessible and efficient (Vázquez-Arellano et al., 2016). A stereo camera is a type of 3D sensors estimating depths based on the principle of triangulation. As a stereo camera simulates a human binocular vision, it gives a machine an ability that humans have. In this study, the stereo camera is applied to detect ridges and furrows for an auto guided planting system. Although the stereo camera has an advantage in outdoor field environments which contain well textured

scenes, stereovision-based applications in agriculture face some challenges in achieving robustness to dynamic scenes caused by a machine movement under uneven surface conditions and changes in texture characteristics disappearing due to varying sunlight conditions.

1.2. Purpose of Research

The goal of this paper is to develop a stereovision-based ridge detection and tracking system adopted in agricultural field conditions. A novel algorithm to detect ridge and furrow is proposed to extract guidance components and navigate a vehicle. Through two feasibility tests under sunlight conditions during a day and in a dynamic situation moving over an uneven surface, the developed algorithm is evaluated by an image classification accuracy analysis. Furthermore, A field test platform is set by applying the developed algorithm to a newly built auto-steering riding cultivator, and field tests is runt to verify the potential of the system for practical real-time application.

1.3. Review of Literature

Stereovision based previous works in agricultural application had an effort to calibrate 3D data by camera extrinsic parameters for a stable object detection. Kise et al. (2005) identified a crop height profile using a stereo camera and a navigation point using a cosine function based cross correlation model. To generate the crop model, an inter-row space of crop field was determined, and it required to be reconstructed for elevation map. Hanawa et al. (2012) developed a stereovision-based auto guidance system by tracking a marker trace using projected bird's eye images. Zhang et al (2018) projected each disparity values on 3D coordinate system using a set of fixed camera extrinsic parameters for the transformation matrix to identify crops rows using a stereo camera. In order to use 3D reconstructed data and the bird's eye images, the previous studies employed initially-defined camera's calibration values. Since their methods required extrinsic camera parameters such as pitch angle, roll angle, and camera installation height, it was hard to actively respond to dynamic vehicle movement on rough surface of the field, unless the extrinsic camera parameters would be estimated in real-time.

Blass et al. (2011) suggested a more practical method in use of stereovision-based auto guidance system under conditions on uneven and/or hilly ground. The swath detection method developed by Blass et al. (2011) for an auto-guided baling system defined the swath region in depth image by searching a ground plane using RANSAC plane fitting method. This

method, however, is difficult to apply in ridge and furrow environment because there is no apparent ground plane which would take a form of nearly flat horizontal conducting surface and take up a relatively large region in an image. The v-disparity presentation, introduced by R. Labayrade and D. Aubert, is widely used to configure the ground surface plane for stereovision based off-road vehicle navigation (Broggie et al., 2005 & Soquet et al., 2007 & Zhao et al., 2007 & Chen et al., 2008 & Shrivastava et al., 2019). We introduced the row-by-row binarization method to classify ridge and furrow previously (Yun et al., 2018). The v-disparity representation and the row-by-row binarization method were used in processing the images of row by row. The methods had little impact on longitudinal variations caused by pitch movements. Strong roll angles variations, however, could still cause poor performance. Herghelegiu et al. (2016) points out the importance of roll angle in use of the v-disparity representation and confirm the effect in simulations. In this paper, the use of a combination of an appropriate use of the v-disparity representation and a proper roll angle compensation method is proposed to respond to both erratic pitch and roll movement in ridge and furrow environment.

Another difficulty for an outdoor application is controlling it over lighting conditions. Sunlight could cause loss of color information by generating reflection light and cast shadow. Halation regions appearing white in an image caused by reflected light is unpredictable in outdoor environments, because the direction of the sunlight is changing over time and the angle of the reflected light, which causes the halation, is varying from place to place

(Nishiwaki et al., 2006). Hanawa et al. (2012) also points out the limitation of utility of the stereo camera due to partly projected shadow casted by a strong sunlight. The white region caused by halation or the black region caused by cast shadow remove texture from an image. Since the weak information of the image texture provides insufficient local matching evidence to estimate range information, the stereo camera easily generates the outliers' measurements in outdoor environments.

Chapter 2. Materials and Methods

2.1. Ridge and Furrow

In furrow irrigation, the soil is raised and lowered at regular intervals so that the water drains well, the area where the crops grow are well-lit and the roots breathe easily before the seed is sown. This microtopography of the soil formation is called corrugation as in Fig.1. The corrugation is divided into the upper part of which the crop is planted and the lower part where the water drained, which is called ridge and furrow, respectively. Since the purpose of this research is the development of auto-guidance method for riding type agricultural vehicle, the ridge and furrow should be defined based on

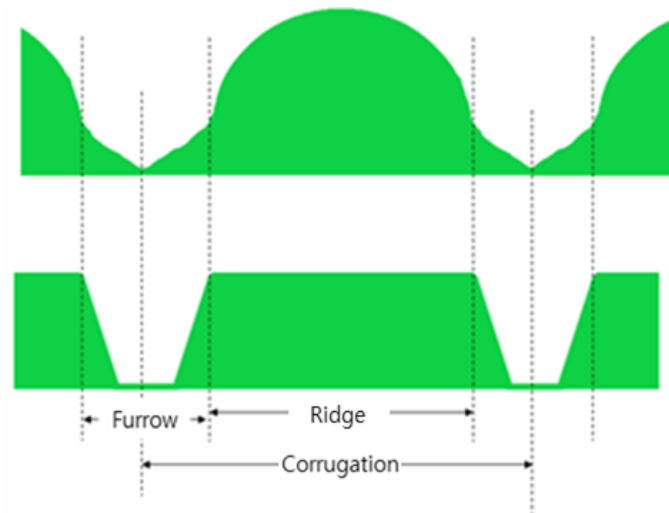


Fig. 1 Corrugation, ridge and furrow



Fig. 2 Dimension of the 15kW riding cultivator developed by TYM

mechanized operations. The size of corrugation is normally set according to the size of the vehicle, implement and type of crop. Fig.2 shows the dimension of the vehicle used in this research. In the aspect of vision-based detection, however, depending on methods of ridge formation, the detection methods could bring up different ideas. If the corrugation is formed simply by ridgers, the color difference between ridge and furrow appears due to the difference in soil moisture content. In the modern ridging method for seeding, in order to make the soil surface soft and even, the ridging process is mostly accompanied with pulverization and bed shaping. These processes make the color of soil surface uniform. Considering various corrugation environment, using the height different between ridge and furrow is most reasonable to determine the traversable pathway.

2.2. Principle of Stereovision

Stereovision simulates human binocular vision by using the principle of triangulation. A single digital camera in which photoelectric sensors are arranged in two-dimensional array capture color information from a scene and record discrete values in a digital image. Each pixel in the image represents the color of a projection ray from an object passing through the optical center. With 2D array images alone, however, it is not possible to estimate the position of the object as all points of the projection ray can be projected on the same pixel. Otherwise, two cameras separated by a known distance and fixed parallel one to another captures the same object scene, and two projection rays projecting on each image from the same object point forms a triangle. The plane where the triangle lies is called the epipolar plane. The line between the two cameras' optical centers, O and O' , is called baseline (Fig. 3). The intersection between the baseline and each plane is the epipole. The line passing through the projection point and the epipole is

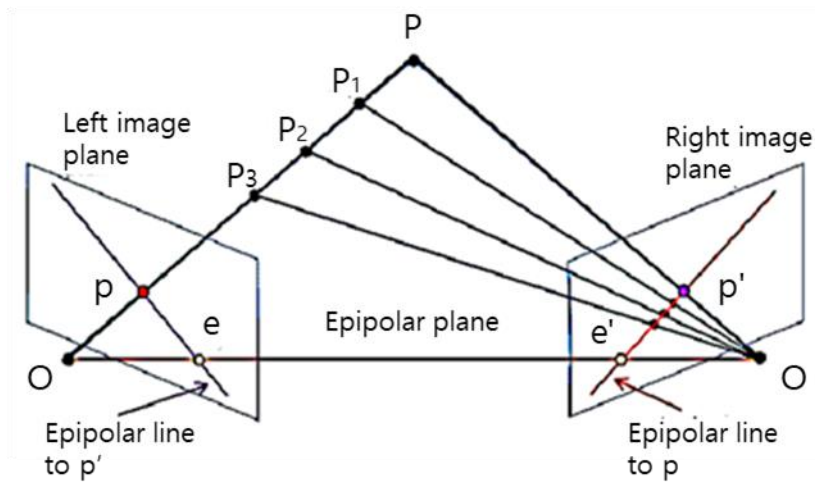


Fig. 3 Stereovision (“Image rectification”, 2019)

the epipolar line. The epipolar line can also be defined as the line of intersection between the epipolar plane and the image plane. The location of the projection points on the epipolar line, therefore, determines depth information of the object. Since the two projection points are projected from the same object point, the local neighborhoods of stereo images take a similar texture information. A pair of corresponding points in stereo images is indicated using feature matching techniques. The process of triangulation recovers three-dimensional information of the object point; this is called stereo matching. A pair of images taken from the slightly displaced camera lens is distorted and unrectified in real world. Before the process of stereo matching, the distorted and unrectified images are required to be transformed onto a common image plane and bilinearly interpolated; this process is called rectification (Fig. 4). Through the rectification, all epipolar lines become parallel to the baseline. Disparity between two matching corresponding points on an epipolar line represents the distance in pixels. One of the pair of images is set as the reference image and a disparity image corresponding to the reference image is obtained. The disparity image is a

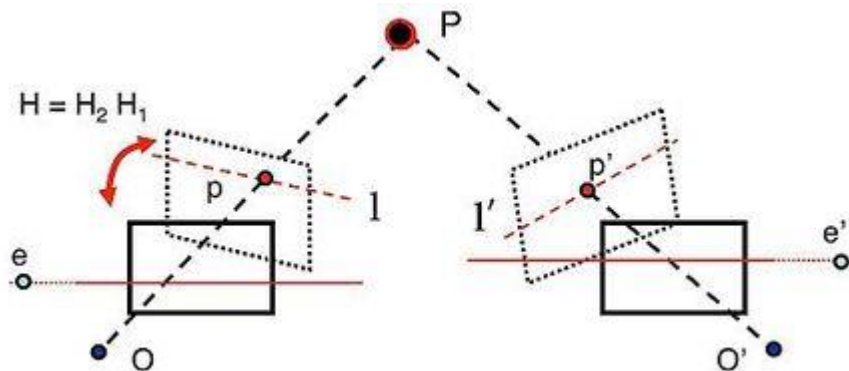


Fig. 4 Rectification (“Image rectification”, 2019)

2D array that stores disparity values expressed in pixel and contains three-dimensional information. The stereovision gives the fine estimation of the position of objects in the scene. Because of the process of stereo matching, the performance of stereo cameras depends on its method and environmental conditions such as white walls and specular areas which generate homogenous and textureless regions in the image. Nevertheless, the rich information based on the relatively high resolution, density and co-registered color images of stereo cameras facilitates their use in various applications (Szeliski, 2010).

2.3. Ridge and Furrow Detection and Tracking Algorithm

Under an uneven field surface condition, erratic movements of camera make difficult to interpret 3D data. The erratic movements are specified into pitch oscillation and roll oscillation. The proposed algorithm shown in Fig.5 is designed to robustly classify the disparity image into ridge and furrow regions assigned to binary, without affecting the camera's oscillations and extract a guidance line from the binary image. The disparity images have been provided by Stereolabs ZED SDK, and the algorithm is implemented using C++ and OpenCV library.

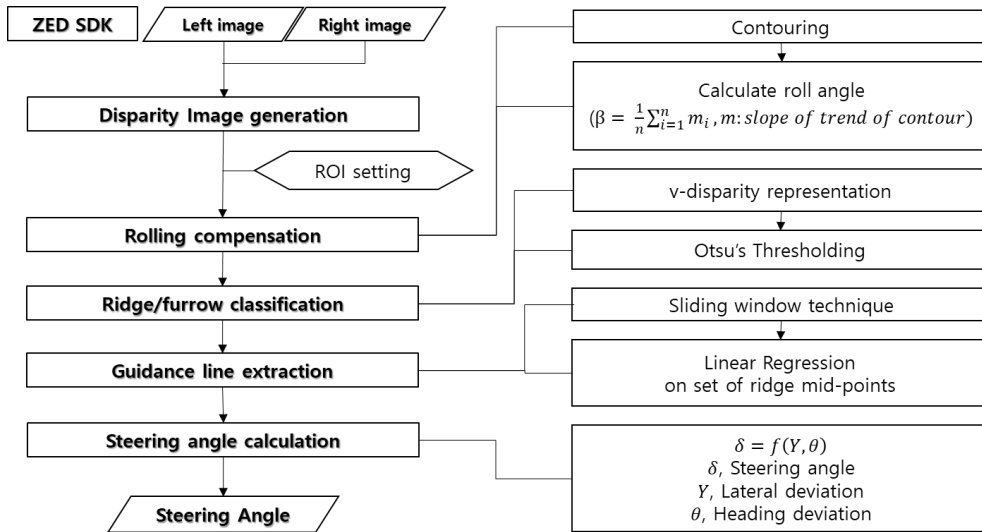


Fig. 5 Ridge-furrow detection and tracking algorithm

2.3.1. Ridge and furrow classification algorithm using v-disparity and Otsu's thresholding

First, to classify the disparity image into ridge and furrow regions, a proper binarization process is required in consideration of the pitch oscillation. The v-disparity representation is a useful method to describe a longitudinal profile of non-flat surface (Labayrade et al, 2002). Since surface takes up most of the visual field in common outdoor environments such as road, park, and field, the disparity values of the ground surface, which occupies the most fraction of the image, emerges as the peak in a histogram of each disparity image row. A slanted line, therefore, generally appears on where the ground surface exists in the v-disparity map (Broggi et al., 2005 & Soquet et al., 2007 & Cong et al., 2010). Broggi et al. (2005) defined it as “ground correlation line”. Unlike other environment surfaces, since there is no representative ground plane in ridge and furrow environment, the v-disparity image taken in ridge and furrow environment appears with widely spread and dim lines (Fig. 6c). Instead of segmenting the ground correction line, looking deeper into the v-disparity image (Fig. 7b), each row of v-disparity image returns a shape of

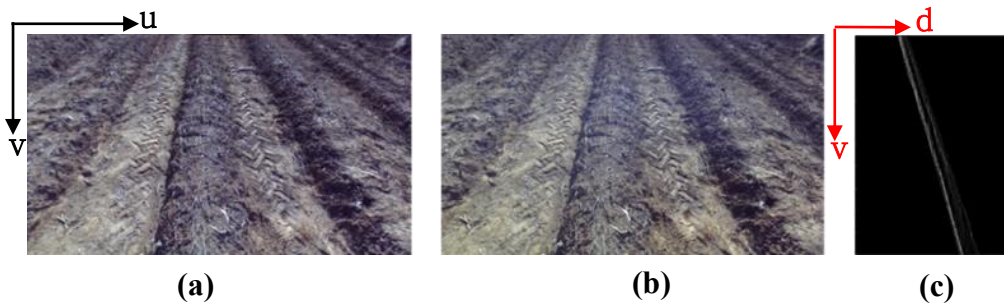


Fig. 6 (a) Left image (b) Right image (c) v-disparity image

bimodal distribution (Fig. 7c) (Broggi et al., 2005 & Soquet et al., 2007 & Cong et al., 2010). The two groups at each peak in the bimodal distribution are included in ridge region and furrow region respectively. Otsu's method, which is known to function rigidly to find a threshold value with a histogram of bimodal distribution, is used to separate pixels into ridge and furrow regions in each row of v-disparity image (Yuan et al., 2015). By applying Otsu's thresholding to all rows of the v-disparity image, the resulting binary image of Fig. 8 which indicates the location of ridge and furrow could be obtained. This way, the proposed algorithm provides effective discrimination capability between ridge and furrow without the pitch oscillation effect.

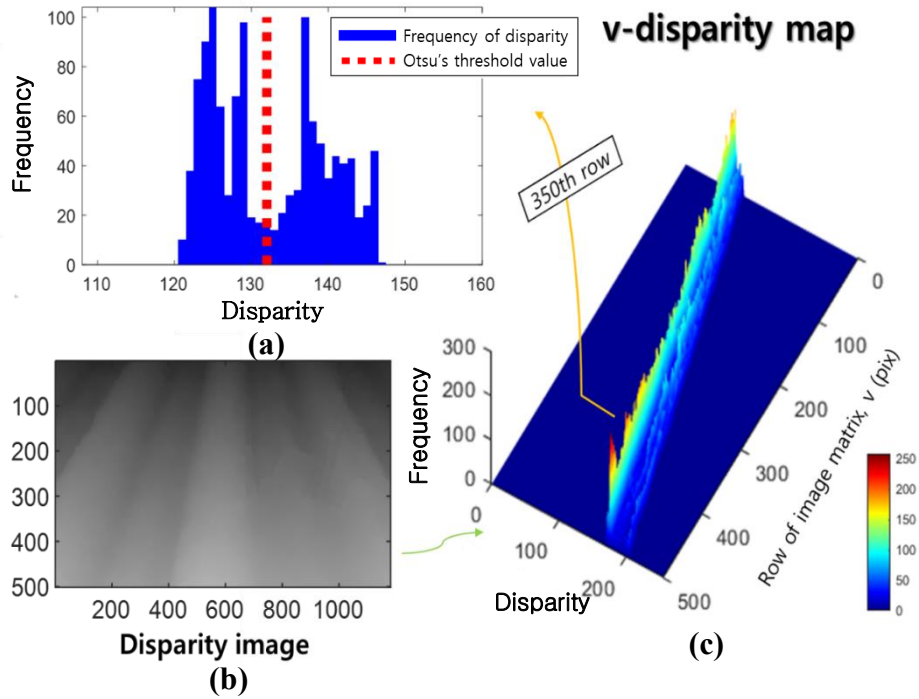


Fig. 7 Ridge and furrow classification using v-disparity map and Otsu's method (a) A row in v-disparity map (b) Disparity image (c) v-disparity map

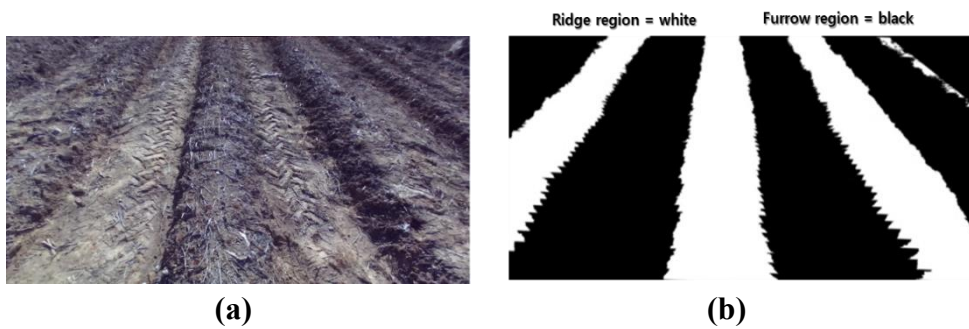


Fig. 8 (a) Color image - left (b) Binary image of ridge and furrow

2.3.2. Roll angle compensation

The rolling oscillations occurred by vehicle movement over uneven surfaces makes each row of the disparity image appear to follow a non-horizontal pattern (Fig.9b). This profile deformation negates the previous classification step because the single threshold value is unable to slice the boundary of ridge and furrow (Fig.9). The suggested solution for this problem is to reversely rotate the image as much as the camera is horizontally tilted with respect to the ground surface, so that the image x-axis turns to become parallel to the surface profile. This is called a relative rolling offset. In order to determinate the relative rolling offset, trend surface analysis is performed using isolines that connect points of equal disparity values (Fig. 10a). The disparity image should be previously blurred by computing the local mean of

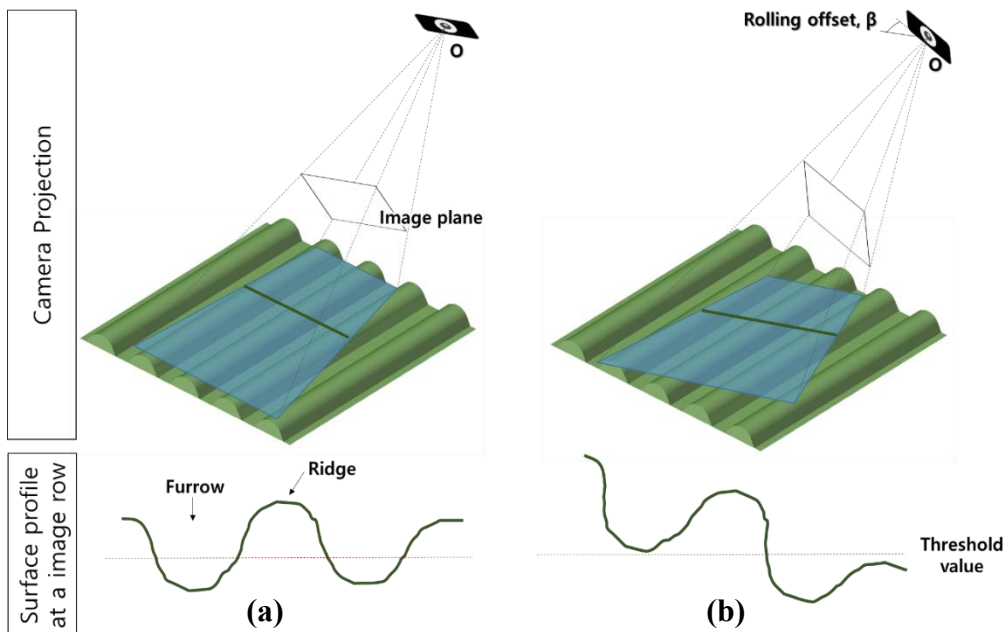


Fig. 9 Image projection problem caused by a rolling offset

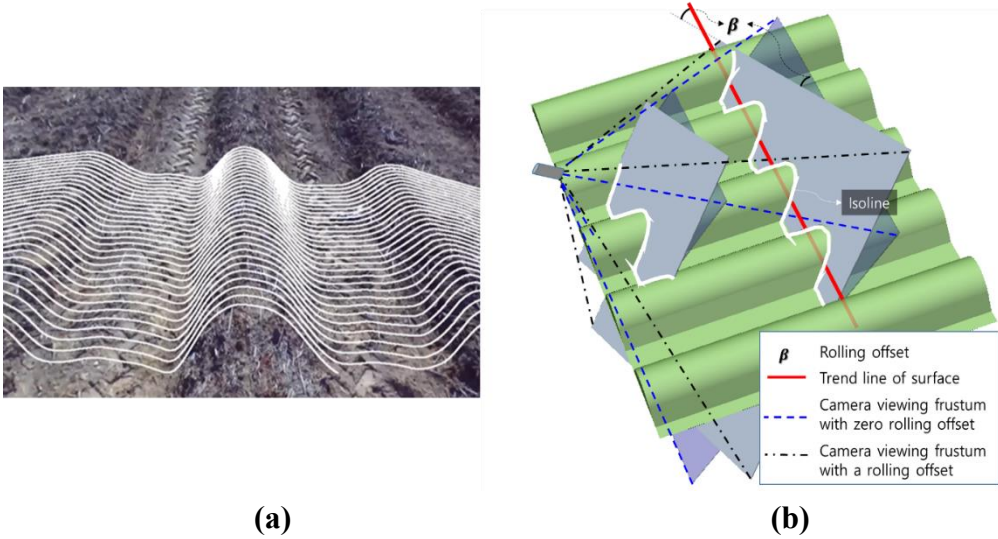


Fig. 10 (a) Plot of disparity isolines in image coordinate (b) Geometric relationship between the isolines and rolling offset

the neighborhood area with the kernel size of 7 by 31 pixels, to remove high frequency components in the disparity image before drawing the isolines. A slope of linear trend of each isoline in the image coordinate is approximately equal to the rolling offset, as the geometrical relationship shown in Fig. 10b. Since points on an isoline indicate surface spots which are equidistant from the principal plane of the camera and located on a slice plane parallel to the image plane; the angle between the image x-axis and the trend line is corresponding to the rolling offset, β , (Fig. 10b). The average slope of all trend lines in one image is used as the image rotation angle, and the rotated disparity image becomes adequate to apply the proposed ridge and furrow classification method. After that, by rotating the image back, the final resulting binary image is aligned with the original position. The overall process of the algorithm is possible to successfully classify ridge and furrow for any movements of the vehicle.

2.3.3. Sliding window technique

Once a binary image is obtained by the previous processes, the position of middle points of the center ridge is collected using row-wise sliding window technique shown in Fig.11 (Fan et al., 2011). The row-wise sliding window technique starts at the bottom row. Both sides of initial sliding windows are set to the width of half the bottom row width and the height set to one pixel. The ridge boundary points are searched at where the nearest change point from each window middle exists. Each ridge boundary point becomes the window middle of the next row, and the width of the next window on both sides is defined as the half-length between the ridge boundary points. The ridge midpoints are collected by searching the center position of the two ridge boundary points on each row (Fig. 11). Finally, the guidance line is extracted by applying linear regression to the set of ridge midpoints. This way, whether the path on ridge and furrow is straight or slightly curved, the guidance line is robustly extracted from the binary image.

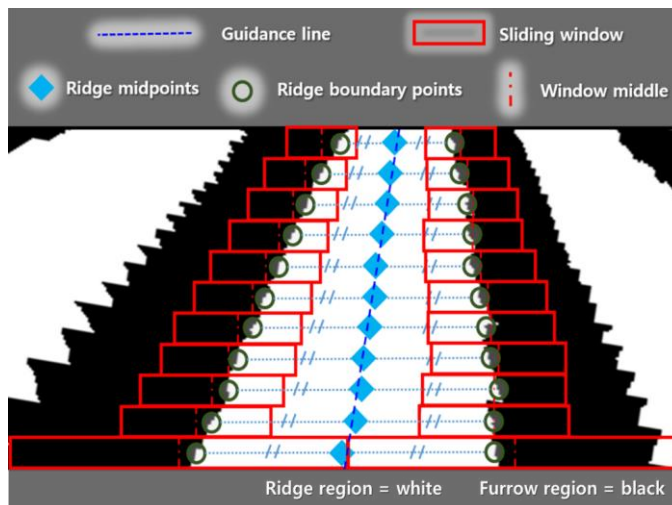


Fig. 11 Guidance line extraction using sliding window method

2.3.4. ROI Setting

Setting Region of Interest (ROI) is also an important part to reduce potential errors in use of disparity images. ROI functions to cut unnecessary regions off. The first part of the cutoff is border occlusion regions. Since some of the portion is captured out of the overlap between the two lenses from the field of views, the occlusion is easily generated at the border area of an image (Fig. 12b) (Huq et al., 2013). Even though the occlusion filling algorithm provided by ZED SDK in Fig.12c also estimates missing disparity values occurred by both, border occlusion and non-border occlusion, it is still better to remove the unreliable regions at the borders. The second one is unreliable range regions. At far detection ranges, it is hard for the stereo camera to estimate range values. Therefore, the stereo camera reliability diminishes due to its resolution and the limited baseline length. Otherwise, objects approaching the camera too close, due to an excessive pitch movement or some parts of vehicle structures, are possible to be captured at the bottom region of the image, based on the installed location. The shape of ROI looks like in Fig.12a.

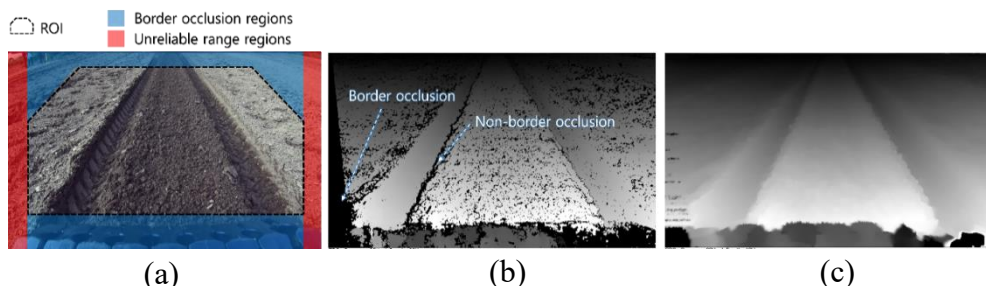


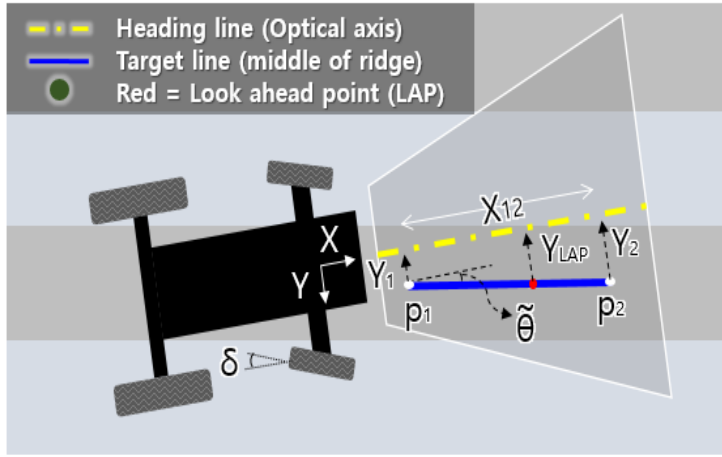
Fig. 12 (a) Region of Interest, ROI (b) Disparity image without occlusion filling (c) Disparity image after applying occlusion filling

2.3.5. Path Tracking model

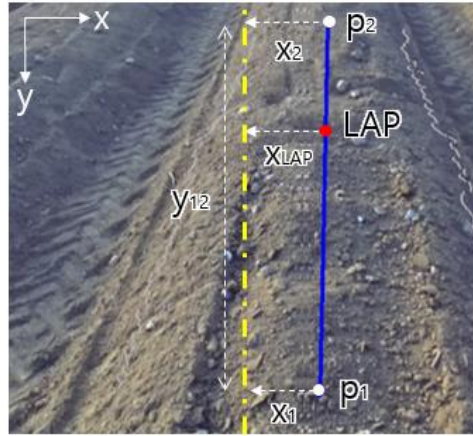
Once the guidance line is extracted by the previous processes, the final stage of the developed method determines the steering angle of the vehicle. The steering angle of vehicle (δ) is calculated by the PD control-based Ackermann kinematic model (Lenain et al., 2007):

$$\delta(Y, \theta) = \tan^{-1} \left(L \left[\frac{\cos^3 \theta}{(1 - Yc(s))^2} (-K_d(1 - Yc(s)) \tan \theta - K_p Y + c(s)(1 - Yc(s)) \tan^2 \theta) + \frac{c(s) \cos \theta}{1 - Yc(s)} \right] \right) \quad (1)$$

where L is the vehicle wheelbase, K_d is the derivative gain, K_p is the proportional gain and $c(s)$ is the curvature of a path. The variables of t Eq. (1) are lateral and angular deviation, respectively Y and $\tilde{\theta}$, which can be calculated from the obtained guidance line, also defined as target line (Fig. 13). Fig. 13a shows the schematic top view of the tracking field, the XYZ coordinate system is defined on a metric space. The lateral deviation of the tracking model is defined as the perpendicular distance of the look ahead point from the X-axis, which is Y_{LAP} . The lateral deviation at the look-ahead point, x_{LAP} , in Fig. 13b, is defined in a pixel coordinate system, xy. The pixel distance of the look-ahead points perpendicular to the heading line. The heading line in the image, which is indicating the travel direction of the vehicle as well as the principle line of the camera, should be aligned to the X-axis when the camera is installed on the vehicle and rigidly mounted. In order to calculate the lateral deviation by reading the pixel distance, the relationship between the disparity value, d , and the metric distance value, D , is required.



(a)



(b)

Fig. 13 Guidance line schematic (a) projected field view (b) Components on the image

The equation is:

$$D = \frac{f \cdot T}{d} \quad (2)$$

where f is focal length, and T is the length of baseline of the stereo camera.

As the geometric relationship shown in Fig. 14b, the lateral deviation is defined as following equations:

$$Y = Y_{LAP} = \frac{D_{H_LAP} \cdot x_{LAP}}{f} = \frac{T \cdot y_{LAP}}{d_{H_LAP}}, \quad Y_1 = \frac{T \cdot y_1}{y_1}, \quad Y_2 = \frac{T \cdot y_2}{d_2} \quad (3)$$

where Y = Lateral deviation for the Eq. (1) (cm),

Y_{LAP} = Lateral deviation of the point on the heading line at LAP (cm)

D_{H_LAP} = Distance between the camera and the point on the heading line at LAP (cm)

d_{H_LAP} = disparity value the point on the heading line at LAP (pix)

Y_1 = Lateral deviation of the point, p_1 , in Fig.13a (cm)

Y_2 = Lateral deviation of the point, p_2 , in Fig.13a (cm)

y_1 = Lateral deviation of the point, p_1 , in Fig.13b (pix)

y_2 = Lateral deviation of the point, p_2 , in Fig.13b (pix)

To calculate the angular deviation, the projected distance of the field of view, X_{12} , is required as well as two lateral displacement parameters, Y_1 and Y_2 , obtained from Eq. (3). Fig. 14a shows the relationship between the projected distance and the camera's vertical angles. Eq. (4) defines the relationship between the measured distances and the vertical angles at points p_1 and p_2 :

$$h = D_{H1} \cos(\alpha_1) = D_{H2} \cos(\alpha_2) \quad (4)$$

where D_{H1} is the distance value at the point perpendicularly dropped from p_1 to the heading line, D_{H2} is the distance value at the point perpendicularly dropped from p_2 , α_1 is the vertical angle between the Z-axis and the projection axis to p_1 , and α_2 is the vertical angle between the Z-axis and the projection axis to p_2 . Using the relationship between the vertical angles and the vertical field of view of the ROI, fov_v , Eq. (4) is solved by the following equations:

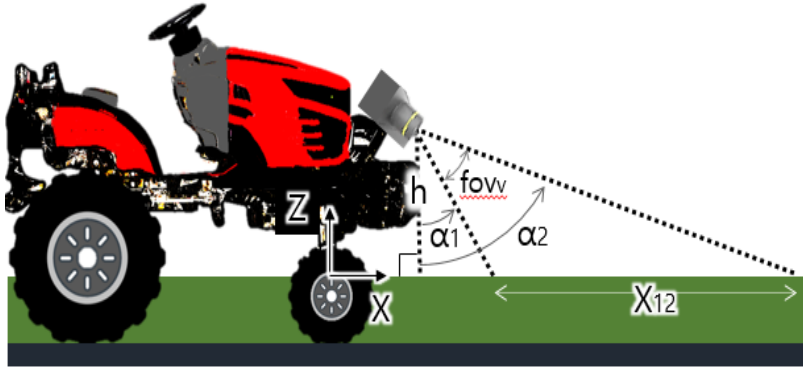
$$\alpha_2 = \alpha_1 + fov_v \quad (5)$$

$$\alpha_1 = \text{atan} \left(\frac{\cos(\text{fov}_v) - \frac{D_{H2}}{D_{H1}}}{\sin(\text{fov}_v)} \right) = \text{atan} \left(\frac{\cos(\text{fov}_v) - \frac{d_{H1}}{d_{H2}}}{\sin(\text{fov}_v)} \right) \quad (6)$$

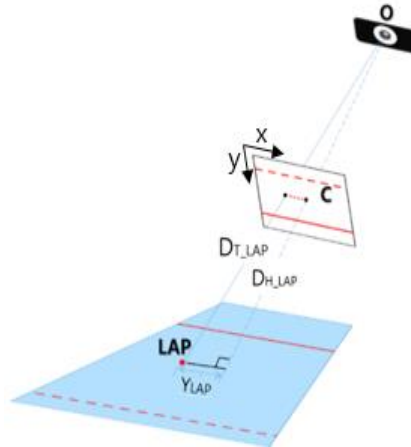
The angular deviation of Eq. (1) is calculated by the following equations:

$$X_{12} = D_{H2} \sin(\alpha_2) - D_{H1} \sin(\alpha_1) = f \cdot T \left(\frac{\sin(\alpha_1 + \text{fov}_v)}{d_2} - \frac{\sin(\alpha_1)}{d_1} \right) \quad (7)$$

$$\theta = \text{atan} \left(\frac{Y_2 - Y_1}{X_{12}} \right) \quad (8)$$



(a)



(b)

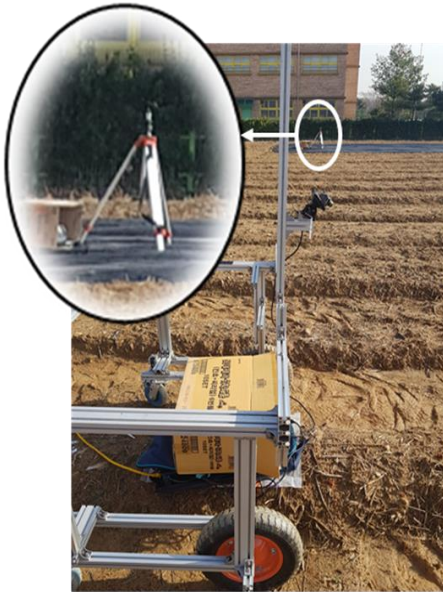
Fig. 14 Geometric relations between the camera, the vehicle and the surface (a) side view (b) 3D view

2.4. Feasibility Tests

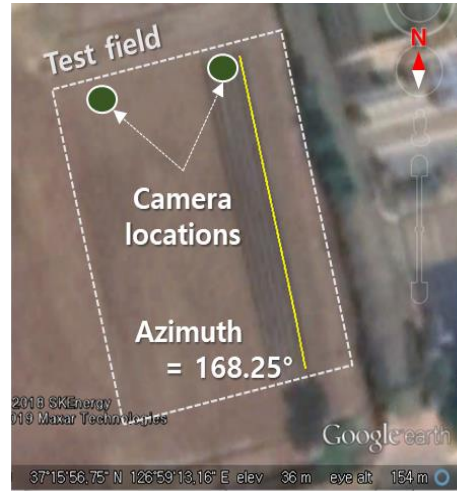
2.4.1. Data Collection

First, to evaluate the developed system under harsh lighting outdoor condition, a set of video data of stereo images were collected from 11am to 5:30pm on a sunny day, when harsh sunlight and cast shadow would occur; for 20 seconds interval, in two different ridge and furrow environment, (which are for bare ridges and mulched ridges), at the same time (Fig.15(a)). The ridges were manually formed in a rounded shape with height of 20cm and width of 80cm, along an azimuth about +168 degree measured using Google Earth Pro (Fig. 15b). The peak illuminance reached about 60,000 Lux at 1:00pm (Fig. 15c).

Then, to evaluate and simulate a vehicle's dynamic situation, a set of video data of stereo images was collected during a stereo camera installed cart, shown in Fig. 15a, travelling over 30m length of ridges and furrows on a sunny day. The stereo camera was mounted on a cart, one meter above the ground, which was drawn manually. Although the cart was lighter than any other real agriculture vehicle, and fluctuating more than real applications, the data collected with it was useful to evaluate and simulate the feasibility, even under rough conditions.



(a)



(b)



(c)

Fig. 15 Image collecting environment (a) Camera installation (b) Google Earth view of the test field (c) Illuminance during day hours

2.4.2. Image Classification Accuracy Analysis

To evaluate a ridge-furrow classification performance of the developed algorithm, pixel-wise classification accuracy was assessed in comparison to manually-labelled ground truth data. The evaluation program is designed that an assessor discerns boundary lines between ridge and furrow by reading the corresponding RGB image. Based on the designated boundary lines, pixels on ridge regions are set to white value, and pixels on furrow regions are set to black value. The accuracy measurement is useful to provide a quantitative evaluation result (Reina et al., 2016). The classification accuracy is defined as:

$$Accuracy = \frac{TP + TN}{(TP + TN + FN + FP)} = \frac{TP + TN}{\text{Number of all pixel in ROIs}} \quad (4)$$

Where TP = True positive, number of ridge pixel in ridge region

TN = True negative, number of ridge pixel in furrow region

FP = False positive, number of ridge pixel in ridge region

FN = False negative, number of ridge pixel in furrow region

For the feasibility test on daylight condition, approximately 2300 images of both bare ridge and mulched ridge were evaluated and manually-labelled once for each set of videos. Concerning the feasibility test for dynamic situation, since every image in the collected video have different orientations, the ground truth data was generated by manually-labeling at each image. The evaluation program helped to analyze the data efficiently.

2.5. Field Testing

2.5.1. Ridge Tracking System

The test platform used for ridge tracking was a 15kW prototype intelligent riding-type cultivator provided by TYM. The riding-type cultivator is a straddle tractor which has an extensive ground clearance, 530mm, and is suitable for inter-row cultivation in Korea, where most farms are small. The developed ridge tracking system is designed to track the ridge located at the center of a vehicle and used to track a path for potato seeding (Fig.16). The ridge tracking system is used to track a path for potato seeding as in Fig.16. The major components of the auto tracking system are a stereo camera, an embedded workstation and an electric power steering installed like shown in Fig. 16. The ZED mini stereo camera used in this research provides a software development kit which can capture 3D videos at resolution of 720p and frame rate up to 60fps (Stereolabs, 2019). Since the ZED stereo camera requires CUDA to compute the disparity image in real-time, the embedded workstation is equipped with Quadro P3000. The other parts of the algorithm are implemented in CPU environment using C++ and OpenCV library. The steering angle computed in the workstation is sent to an ECU board in Electric Power Steering (EPS) via CAN bus and is updated in 5Hz. In order to evaluate the tracking performance of the developed system, a dual GPS INS composed of a Novatel OEM-617-D GPS receiver with dual antennas and an SBG Ellipse2-D inertial sensor, mounted on the top of the riding cultivator, was used to measure the tractor's accurate location with a VRS-

RTK connected to the GPS data link via the workstation (Fig.16).

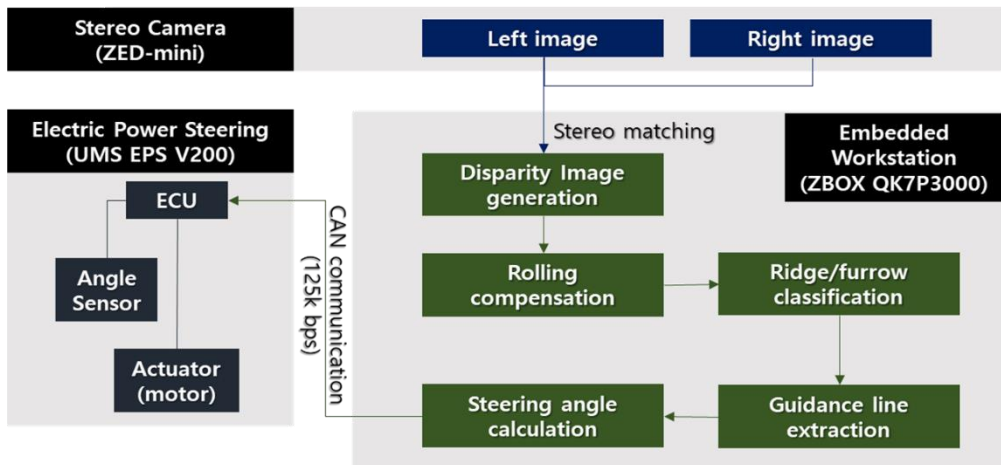
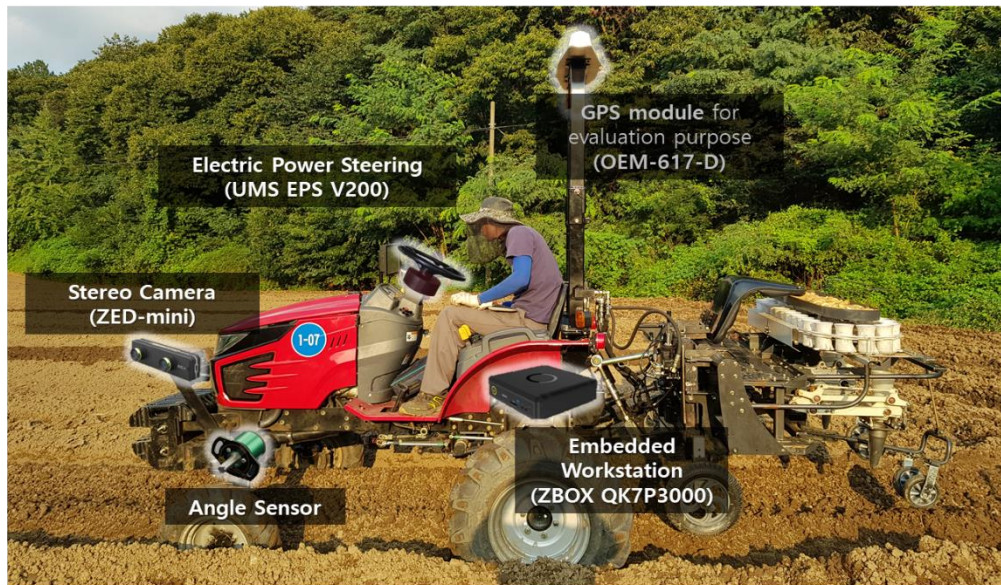


Fig. 16 Stereovision based ridge tracking system overview

2.5.2. Test Fields and Performance Evaluation

The ridge tracking tests were run in two different places respectively in May 2019 and in August 2019. The ridges were formed on a nearly flat field in the first place, then on a hilly field. The ridges had a width of 100 cm and height of 20 cm (Fig. 17). To compare the performance of the developed system to human driving, GPS data were collected while the vehicle was travelling over the same ridge path, operating in both auto-guided control and manual control. The collected GPS data output was in the UTM coordinate format (Han et al., 2013).

Since the ridge was not formed perfectly straight and the paths of GPS data were collected at different times, a proper analysis method of the collected GPS data was required to evaluate the tracking performance of the developed system reasonably. The lateral deviation is the displacement of

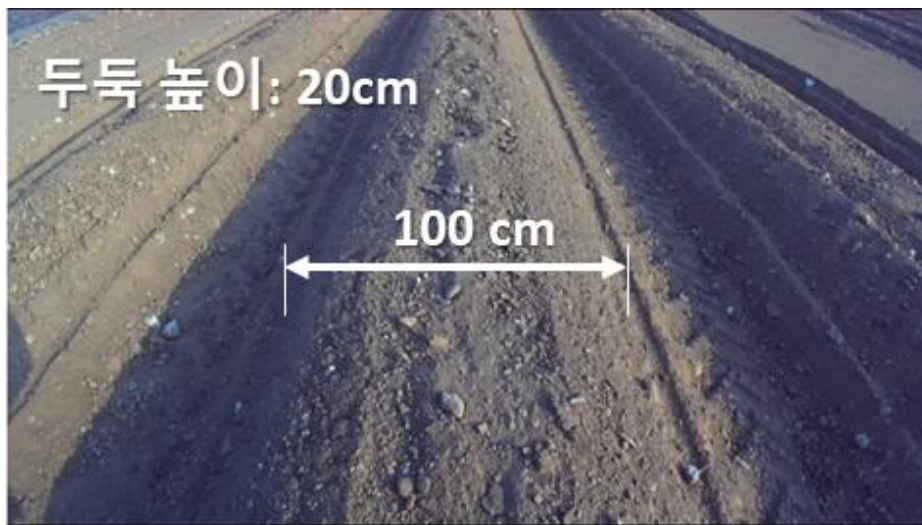


Fig. 17 Size of ridge

the vehicle relative to the target course in the normal direction. In the ridge tracking situation, the target course is the ridge lined pathway. Because it is difficult to calculate the normal vector of every point on the non-straight ridge line, the straight line between the start point (A) and the end point (B) of the manually driven path (Fig.18) was set as reference axis, thus the normal vector becomes uniform. Fig.19 shows the GPS data in latitude and longitude UTM coordinates Fig.20 shows the coordinate with AB line to x-axis, transforming through the translation and rotation. Shown in Fig.20, the GPS point data gap between the manually driven path and the auto-guided path exist. The gap is simply eliminated by filling out intermediate values of the GPS points of the manually driven path through the linear interpolation. As a result, the lateral deviation of every GPS point of auto-guidance paths is calculated corresponding to the manually driven paths

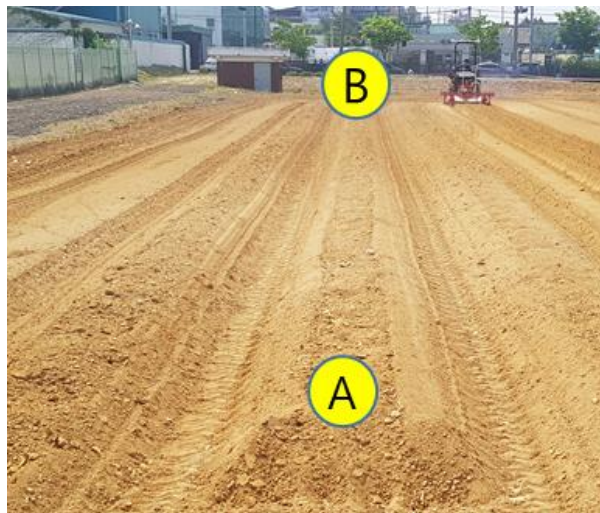


Fig. 18 A and B points on the ridge

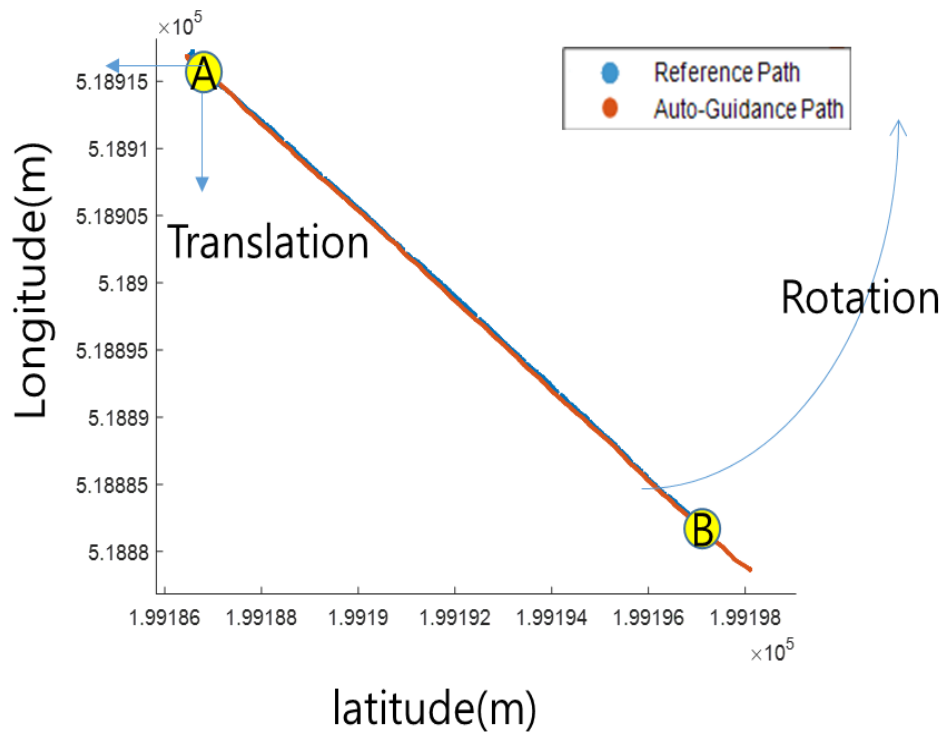


Fig. 19 A and B points in the UTM coordinate

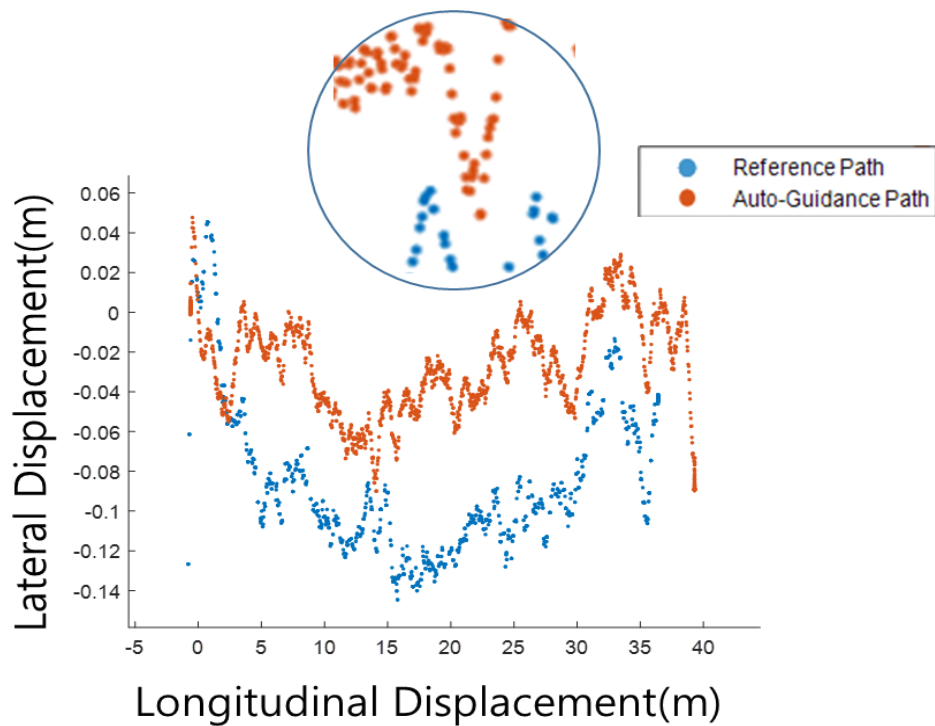


Fig. 20 GPS point data gap

Chapter 3. Results and Discussion

3.1. Effect of Sunlight on Detection Performance

Under daylight conditions, the developed algorithm successfully classifies the ridge and furrow in most daytime (Fig. 21). The standard deviation between the accuracy results by time is negligibly small and relatively steady for both cases (Table 1). However, at certain times, 11:05am, 13:14pm, and 16:00pm, the accuracy in the plastic mulched ridge sharply decreased. 3D projected elevation maps shown in Fig. 22, displays well the cause of error at those specific times. At 11:05am, the region where the halation appears, disparity values collapsed. At 16:00am, the region where shadow is casted, disparity values also collapsed. At 13:14am, both halation and cast shadow

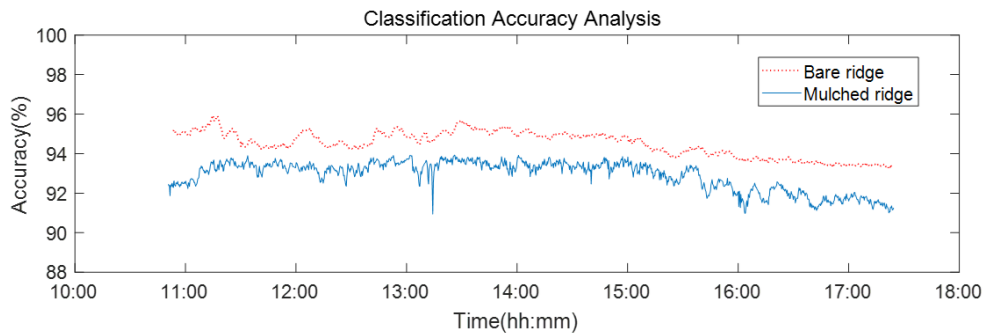


Fig. 21 Feasibility test result under daylight condition

Table 1 Result for the daylight feasibility test

Type of ridge	Average (%)	Standard Deviation (%)	Maximum (%)	Minimum (%)
Bare	94.482	0.636	95.936	93.263
Mulched	92.892	0.742	93.930	90.941

appear at the same time and show minimum accuracy. At the textureless regions in RGB images, caused by lights reflected from smooth surface points, and shades near boundaries between ridge and furrow, the stereo camera is not able to measure reliable disparity values, since the stereo matching algorithm does not perform well (Chang et al., 2016). As the textureless regions in this experiment occupy relatively small areas and other center points at each segment redeem error points, the extracted guidance lines still resulted practically.

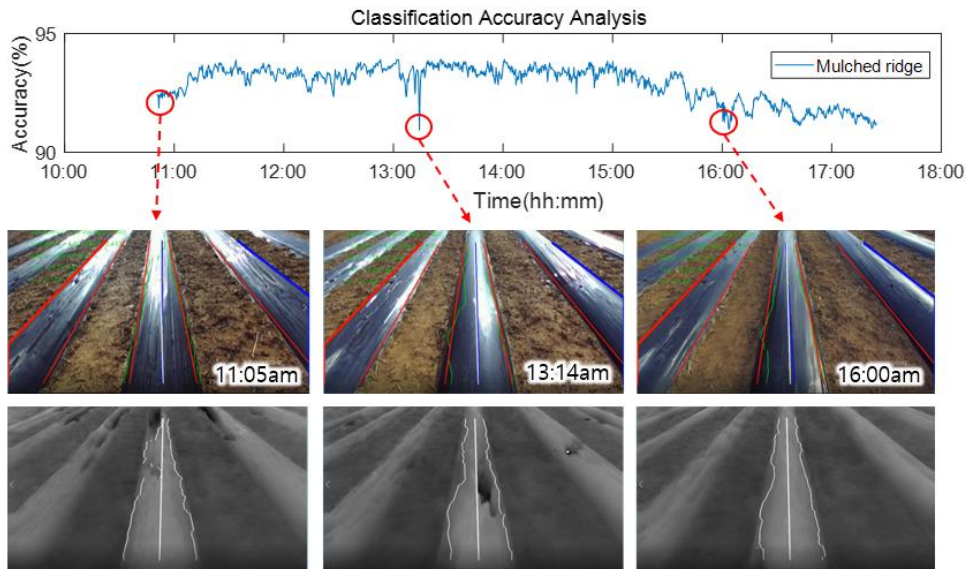


Fig. 22 Errors caused by sunlight

3.2. Feasibility of Using Roll Angle Compensation Method for Uneven Surface Movement

To verify the effectiveness of the rolling offset compensation method, the complete oscillation compensated algorithm was compared with the algorithm using only the ridge and furrow classification without the rolling offset compensation by the accuracy analysis employed on the same image data set. The accuracy results showed that the developed algorithm performed with the average of 93.5% and the standard deviation of 1.62%, while the algorithm without the rolling compensation resulted with a large variation with the average of 89.3% and the standard deviation of 6.68% (Fig. 23 & Table 2). Without the rolling offset compensation, the boundary of either side becomes ambiguous and it would occur an unreliable result to extract a guidance line; an example of it is shown in Fig. 24. It proves the feasibility of the developed algorithm against dynamic movements in the uneven field environment.

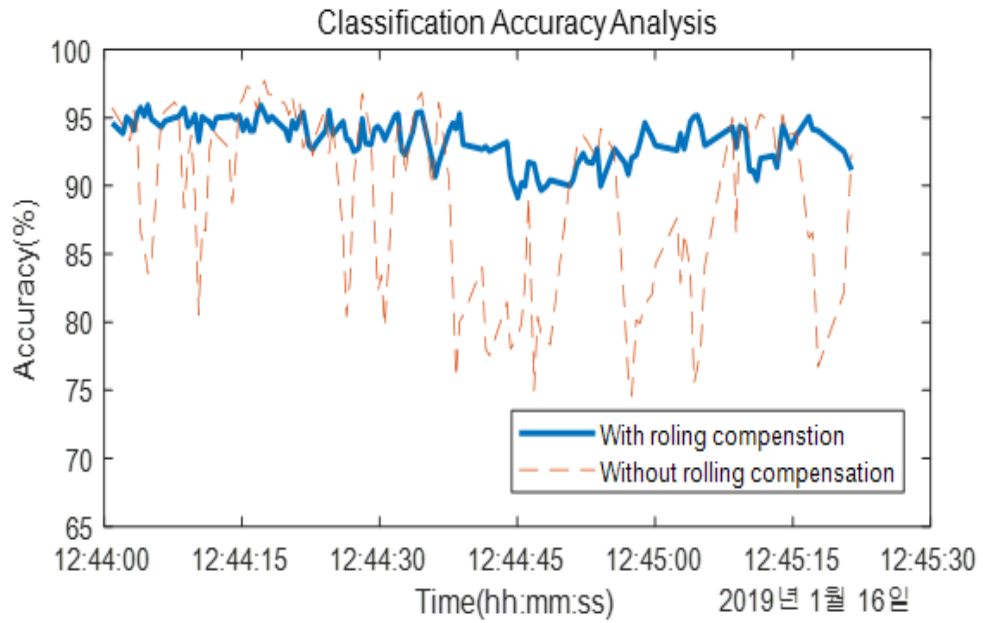


Fig. 23 Feasibility test result under condition of vehicle moving on uneven surface

Table 2 Result for the dynamic situation feasibility test

Algorithm	Average (%)	Standard Deviation (%)	Maximum (%)	Minimum (%)
With Rolling Compensation	93.5	1.62	95.9	89.1
Without Rolling compensation	89.3	6.68	97.7	74.6



(a)

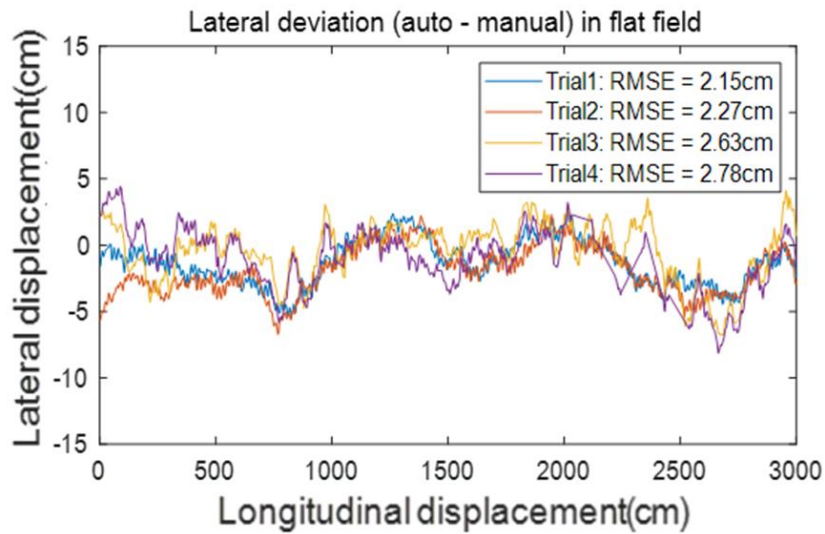


(b)

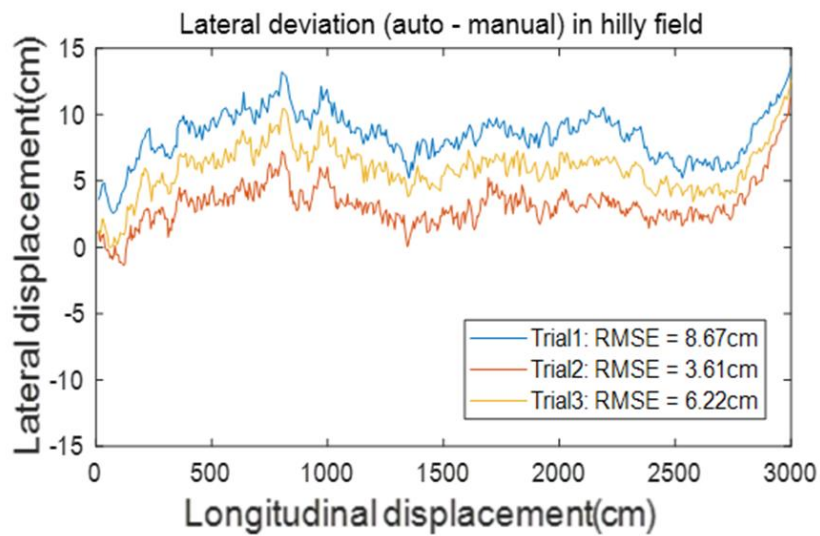
Fig. 24 An example of erratic result of guidance line extraction (a) without rolling offset compensation (b) with rolling offset compensation

3.3. Field Test Result

The RMS results of lateral deviation between the auto-guided path and the manually-driven path show that the developed system performs no different than the human task on flat field. Its values are 2.15cm, 2.27cm 2.63cm, and



(a)



(b)

Fig. 25 Lateral deviation between auto-guided path and manually-driven path on (a) flat field (b) hilly field

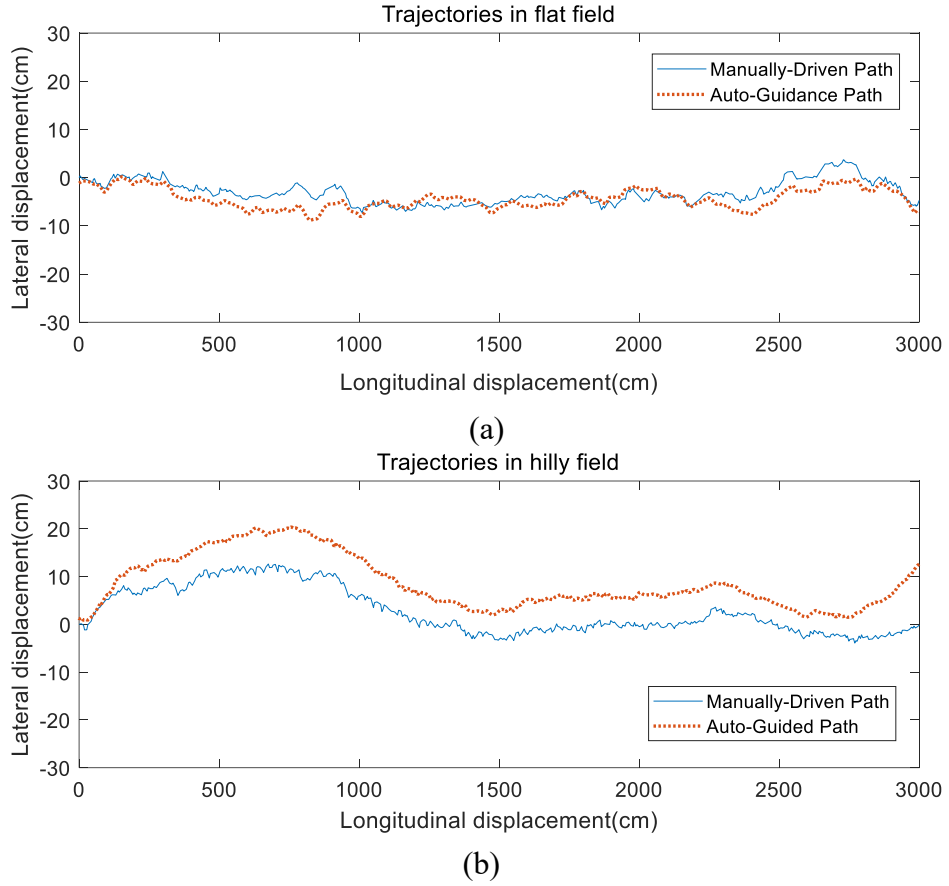


Fig. 26 Trajectory plot (a) flat field (b) hilly field

2.78cm for each of the four trials respectively (Fig. 25a). On the hilly field, the RMS results are larger than the one on the flat field. For all of the three trials, the values are 8.67cm, 3.61cm and 6.22cm (Fig. 25b). This is can be explained by the trajectories of the paths. Also, the auto-guided trajectory on the hilly field have similar pattern with the manually-driven one but move away downhill from it (Fig. 26b). Fig. 27 shows the steering angle command calculated from the developed algorithm. Unlike the flat field case (Fig. 27a), the steering angle command for the hilly field is biased and the direction of it is the clockwise which is opposite to downhill (Fig. 27b). This means the steering angles calculated by the developed algorithm have commanded the

vehicle to move to the direction of uphill, but the vehicle could not conduct the command. To improve the tracking performance, the modified tracking algorithm is required to respond to the side slip at low velocity (Han et al, 2019 & Bell, 1999). The speed of vehicle for the riding cultivator during the tests is evenly about 0.25m/s. Even though there are the small location biases for hilly field tests, overall results show the developed system has been able to robustly trace the inter-row path of ridge and furrow.

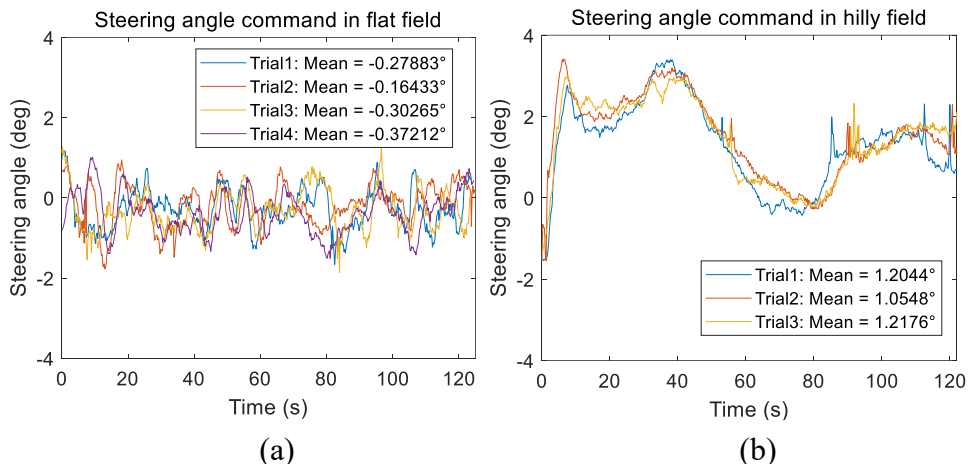


Fig. 27 Steering angle command (a) flat field (b) hilly field

Table 3 RMSE of the ridge tracking result

Type of field	Trial	Velocity (m/s)	RMSE of Lateral deviation (cm)	Mean of steering angle command (degree)
Flat	1	0.25	2.15	-0.28
	2	0.25	2.27	-0.16
	3	0.25	2.63	-0.30
	4	0.25	2.78	-0.37
Hilly	1	0.25	8.67	1.20
	2	0.25	3.61	1.05
	3	0.25	6.22	1.22

Chapter 4. Conclusions

Stereovision-based guidance extraction algorithm for ridge and furrow field is developed using v-disparity representation, Otsu's thresholding, roll angle compensation, and row-wise sliding window approach. The feasibility tests under daylight condition and the dynamic situation were performed using classification accuracy assessment. In ridge and furrow environment, unreliable disparity data collected by the stereo camera was occurring at the white regions by the halation, and at the black regions by the cast shadow in the image. The errors caused by the sunlight appear partly in the image. Using the other reliable data, the guidance line could be extracted robustly. The proposed rolling compensation method has also worked well under the rough surface condition in the harsh testing environment set up by the cart. Overall, the developed algorithm has been proven to handle the rough outdoor conditions and extract the guidance line to trace the inter-row path of ridge and furrow. The field tests are meaningful to verify that the developed algorithm operates satisfactorily within the automatic steering system in real time. The ridge tracking system has successfully traced the straight interrow paths of ridge and furrow, even though it had biased tracking performance on hilly field. For further studies, it would be required to figure out the effect of the slip caused by the side slope on the auto-guided tracking system to improve the path tracking model.

Bibliography

1. Blas, M. R., & Blanke, M. (2011). Stereo vision with texture learning for fault-tolerant automatic baling. *Computers and electronics in agriculture*, 75(1), 159-168.
2. Hanawa, K., Yamashita, T., Matsuo, Y., & Hamada, Y. (2012). Development of a stereo vision system to assist the operation of agricultural tractors. *Japan Agricultural Research Quarterly: JARQ*, 46(4), 287-293.
3. Han, X. Z., Kim, H. J., Moon, H. C., Woo, H. J., Kim, J. H., & Kim, Y. J. 2013. Development of a path generation and tracking algorithm for a Korean auto-guidance tillage tractor. *Journal of Biosystems Engineering*, 38(1), 1-8.
4. Kise, M., Zhang, Q., & Más, F. R. 2005. A stereovision-based crop row detection method for tractor-automated guidance. *Biosystems engineering*, 90(4), 357-367.
5. Lenain, R., Thuilot, B., Cariou, C., & Martinet, P. (2007). Adaptive and predictive path tracking control for off-road mobile robots. *European journal of control*, 13(4), 419-439.
6. Reina, G., Milella, A., Rouveure, R., Nielsen, M., Worst, R., & Blas, M. R. 2016. Ambient awareness for agricultural robotic vehicles. *biosystems engineering*, 146, 114-132.
7. Yun, C., Kim, H. J., Jeon, C. W., & Kim, J. H. (2018). Stereovision-Based Guidance Line Detection Method for Auto-guidance system on Furrow Irrigated Fields. *IFAC-PapersOnLine*, 51(17), 157-161.
8. Zhang, S., Wang, Y., Zhu, Z., Li, Z., Du, Y., & Mao, E. (2018). Tractor path tracking control based on binocular vision. *Information Processing in Agriculture*, 5(4), 422-432.

9. Vázquez-Arellano, M., Griepentrog, H., Reiser, D., & Paraforos, D. (2016). 3-D imaging systems for agricultural applications—a review. *Sensors*, 16(5), 618.
10. Skulimowski, P., Owczarek, M., & Strumiłło, P. (2017, September). Ground plane detection in 3D scenes for an arbitrary camera roll rotation through “V-disparity” representation. In 2017 Federated Conference on Computer Science and Information Systems (FedCSIS) (pp. 669-674). IEEE.
11. Han, X. Z., Kim, H. J., Kim, J. Y., Yi, S. Y., Moon, H. C., Kim, J. H., & Kim, Y. J. (2015). Path-tracking simulation and field tests for an auto-guidance tillage tractor for a paddy field. *Computers and Electronics in Agriculture*, 112, 161-171.
12. Han, X. Z., Kim, H. J., Moon, H. C., Woo, H. J., Kim, J. H., & Kim, Y. J. (2013). Development of a path generation and tracking algorithm for a Korean auto-guidance tillage tractor. *Journal of Biosystems Engineering*, 38(1), 1-8.
13. Zhao, J., Katupitiya, J., & Ward, J. (2007, April). Global correlation based ground plane estimation using v-disparity image. In *Proceedings 2007 IEEE International Conference on Robotics and Automation* (pp. 529-534). IEEE.
14. Chen, Y. L., Sundareswaran, V., Anderson, C., Broggi, A., Grisleri, P., Porta, P. P., ... & Beck, J. (2008). Terramax™: Team oshkosh urban robot. *Journal of Field Robotics*, 25(10), 841-860.
15. Soquet, N., Aubert, D., & Hautiere, N. (2007, June). Road segmentation supervised by an extended v-disparity algorithm for autonomous navigation. In *2007 IEEE Intelligent Vehicles Symposium* (pp. 160-165). IEEE.
16. Broggi, A., Caraffi, C., Fedriga, R. I., & Grisleri, P. (2005, September). Obstacle detection with stereo vision for off-road vehicle navigation. In

- 2005 IEEE Computer Society Conference on Computer Vision and Pattern Recognition (CVPR'05)-Workshops (pp. 65-65). IEEE.
17. Zhao, J., Katupitiya, J., & Ward, J. (2007, April). Global correlation based ground plane estimation using v-disparity image. In Proceedings 2007 IEEE International Conference on Robotics and Automation (pp. 529-534). IEEE.
 18. Cong, Y., Peng, J. J., Sun, J., Zhu, L. L., & Tang, Y. D. (2010). V-disparity based UGV obstacle detection in rough outdoor terrain. *Acta Automatica Sinica*, 36(5), 667-673.
 19. Herghelegiu, P., Burlacu, A., & Caraiman, S. (2016, October). Robust ground plane detection and tracking in stereo sequences using camera orientation. In 2016 20th International Conference on System Theory, Control and Computing (ICSTCC) (pp. 514-519). IEEE.
 20. Labayrade, R., Aubert, D., & Tarel, J. P. (2002, June). Real time obstacle detection in stereovision on non flat road geometry through "v-disparity" representation. In Intelligent Vehicle Symposium, 2002. IEEE (Vol. 2, pp. 646-651). IEEE.
 21. Shrivastava, S. (2019, April). Stereo Vision Based Object Detection Using V-Disparity and 3D Density-Based Clustering. In Science and Information Conference (pp. 408-419). Springer, Cham.
 22. Yuan, X. C., Wu, L. S., & Peng, Q. (2015). An improved Otsu method using the weighted object variance for defect detection. *Applied surface science*, 349, 472-484.
 23. Huq, S., Koschan, A., & Abidi, M. (2013). Occlusion filling in stereo: Theory and experiments. *Computer Vision and Image Understanding*, 117(6), 688-704.
 24. Nishiwaki, K., Kondo, N., Kise, M., Zhang, Q., Grift, T., Tian, L., & Ting, K. C. (2006). Feasibility of using polarizing filters to reduce halation effects during image acquisition in the field. In 2006 ASAE Annual

- Meeting (p. 1). American Society of Agricultural and Biological Engineers.
25. Fan, Y., Zhang, W., Li, X., Zhang, L., & Cheng, Z. (2011, July). A robust lane boundaries detection algorithm based on gradient distribution features. In 2011 Eighth International Conference on Fuzzy Systems and Knowledge Discovery (FSKD) (Vol. 3, pp. 1714-1718). IEEE.
 26. Parajuli, A., Celenk, M., & Riley, H. B. (2013). Robust lane detection in shadows and low illumination conditions using local gradient features. *Open Journal of Applied Sciences*, 3(01), 68.
 27. Chang, Y. J., & Ho, Y. S. (2016). Disparity map enhancement in pixel based stereo matching method using distance transform. *Journal of Visual Communication and Image Representation*, 40, 118-127.
 28. Szeliski, R. (2010). *Computer vision: algorithms and applications*. Springer Science & Business Media.
 29. Image rectification. (2019, November 30). In *Wikipedia*. Retrieved from https://en.wikipedia.org/w/index.php?title=Image_rectification&oldid=927927145

자율파종을 위한 두둑검출 및 추종시스템

윤 창 호

국 문 초 록

자율주행 자동차의 차선 감지 기술 및 자율주행 방제기의 작물열 감지 기술과 같이 차량에서 사용되는 비전 방식의 자율주행은 사람의 눈을 대신하여 차량의 경로를 판단한다. 두둑은 고랑 관개에서 나타나는 밭의 지형적 특성이며 작물열과 같이 평행한 형태로 나지만 작물열과는 다르게 색의 특성이 분명하게 나타나지 않지만 두둑과 고랑의 높낮이 차이를 이용하여 농지내 주행 경로를 판단 할 수 있다. 본 연구에서는 스테레오 카메라를 통해 얻은 3차원 정보를 이용하여 두둑의 높낮이 특성으로 두둑과 고랑을 구분하고 자율주행 트랙터의 주행 기준선을 추출하는 알고리즘을 개발하고자 하였다. 개발 알고리즘의 원리는 스테레오 카메라를 통해 얻어진 두둑 표면의 깊이 이미지가 밭의 거친 표면과 트랙터의 거동에 의해 나타나는 카메라와 지면의 상대적인 변화값을 Blurring 기법과 Contour 라인의 기울기 정보를 통해 예측하고, 이를 얻어진 깊이 데이터에 반영한다. 보정된 깊이 이미지는 v-disparity 방법과 Otsu's Thresholding을 통해 최종적으로 두둑과 고랑을 구분하고 각

Segmentation에 대한 두둑의 중앙값들에 대한 선형 회귀 분석을 통해 최종적인 주행 기준선을 추출한다. 개발된 알고리즘을 검증하기 위하여 실제 두둑 환경에서 취득한 영상 데이터를 토대로 이미지 검출률 분석과 횡변위 오차 분석을 수행 하였다. 개발된 알고리즘의 두둑 검출율 분석 결과 평균 94.2%의 정확도를 보였으며 실제 자율주행 플랫폼에 적용 결과 4.05cm의 추종 오차 성능을 보였다.

감사의 글

석사 과정은 제 인생에서 새로운 즐거움을 알려주었습니다. 생각과 아이디어만 풍부했던 학사 과정을 끝내고 석사 과정을 통해 막연하게 떠오르던 아이디어가 학술적 가치를 품는 녹녹치 않는 과정을 배우고 또한 그 과정이 많은 분들의 도움과 지원이 없이는 힘들었음을 깨닫았습니다.

방향성 없이 의욕만 앞세운 저를 올바른 길로 안내해주신 김학진 교수님께 감사의 인사를 전합니다. 고집이 강한 모습도 이해해 주시고 끝까지 포기 하지 않고 아낌 없는 조언을 주셔서 석사 과정을 무사히 마칠 수 있었습니다. 멀리 내다 보시고 해주신 말씀이 당시에는 이해가 되지 않았지만 돌이켜 보면 다 올바른 방향이었다는 것을 늦게 깨달아 후회도 됩니다. 이런 밑거름 삼아 교수님의 제자로서 더욱 훌륭한 연구자로 발전하는 모습 보여드리겠습니다.

멀리서 큰 의지가 되어 주시고 연구의 학술적 가치를 높여 주신 이원석 교수님, 오랜 실무 경험을 토대로 농업 공학의 적용성 측면에서 많은 조언을 주신 김정훈 교수님, 석사 논문의 심사위원으로서 부족한 부분을 채워주신 이종용 교수님 그리고 김기석 교수님, 그리고 석사 과정 동안 많은 가르침을 주신 서울대학교 바이오시스템전공 교수님들께 감사의 마음 전합니다.

석사 과정 동안 얻은 제 인생의 소중한 재산인 우리 연구실 가족들, 가장 가까이에서 농업의 미래와 연구적 아이디어를 공유하고 때론 힘이 들 때 의지가 되어주어 항상 감사한 마음을 가지고 있습니다. 먼저 가장 가까이에서 연구의 아이디어를 공유하고 같이 고생하는 자율주행 팀 친구들에게 마음을 전합니다. 야외에서 얼굴을 그을려가며 실제 적용 단계에서 오는 많은 고충을 공유하며 좋은 결실을 맺을 수 있도록 많은 조력을 해주어서 너무 감사합니다. 많은 실험 경험을 토대로 실험 설계 단계부터 실험까지 찬우의 도움이 없었다면 이 모든 것을 주어진 시간 내에서 완성 할 수 없었습니다. 항상 열심히 하는 찬우의 모습을 보며 동기 부여도 많이 되었습니다. 이번에 건강한 아들을 얻고 힘든 연구실 생활 동안에도 웃음을 잃지 않고 같이 고생 많이 해준 민석에게도 고마움 마음을 전하며 다들 고생 많았습니다. 사소한 문서 처리부터 논문을 작성하는 팁을 많이 공유해줘 의지가 많이 되어준 우재도 너무 감사하고 박사 졸업을 무사히 마칠 수 있도록 항상 응원하겠습니다. 그리고 우리 연구실 친구들에게 실

천으로 많은 동기 부여주시는 대현 형님이 보여주시는 연구적 열정은 저에게 또한 즐거움과 자극이 되어 주셨습니다. 농업에 대한 헌신과 열정을 보여주는 마음 여린 희조도 즐거운 마음으로 농업의 미래에 대해서 같이 고민해줘서 너무 감사하고 비록 이제는 다른 곳에서 미래를 꿈꾸게 되었지만 항상 응원하고 꼭 하고자 하는 일 잘되기 응원하겠습니다. 이제는 연구실이 아닌 다른 공간에서 활동하는 동욱이의 빈 자리로 인하여 연구실이 다시 삭막해져서 원망이 있지만 그와 같이 한 시간 또한 소중하고 감사했습니다. 연구실 선배이자 사업을 운영하시며 인생의 선배로서 많은 조언을 해주신 종우 형님 이번에 박사 졸업 축하드리고 앞으로도 잘 부탁드립니다. 성실한 모습으로 긍정적인 에너지를 준 정환이, 먼 독일에서 길을 같이하는 창주, 항상 긍정적인 말로 저를 붙돋아 주었던 상진이 그리고 유쾌하게 나잇값 못한 길송이도 같이 했던 시간만큼 시간이 흐른 지금도 좀 더 시간을 함께하지 못해 항상 아쉽고 졸업생으로서 좋은 모습으로 이끌어주어 항상 감사하고 있습니다. 논문과 다른 연구실 친구들의 기억 속 그리고 짧은 만남이지만 연구실의 인연을 통해 자신의 위치에서 저에게 연구실 외의 공간과 교두보 역할을 해주시는 졸업생 한웅철 박사님, 봉진 친구와 희섭 친구 모두 감사합니다.

과제를 수행하면서 조언과 좋은 연구 환경을 제공해주신 동양물산 강영선 소장님, 한종규 팀장님 그리고 생산기술연구원의 김정길 박사님께 감사의 인사를 드립니다. 덕분에 좋은 연구 성과를 얻어 졸업을 하게 되었습니다.

귀찮게 말을 걸어도 항상 친절하게 답해 주시는 대학원 원후회 선후배 연구원 동료 분들께 항상 감사하고 대학원 생활 동안 부족한 저를 많은 측면에서 도움을 주신 모미정 선생님과 조혜경 선생님 감사합니다.

마지막으로 항상 옆에서 응원해주고 지칠 때 힘이 되어 주는 우리 가족, 말이 아닌 삶으로 가르침을 주시는 아버지, 아들 걱정 뿐인 여장부 어머니, 항상 아끼는 동생들 성호, 성재 그리고 세상 가장 중요한 존재인 제 아내 이스리 사랑합니다 그리고 감사합니다.

2020년 1월

바이오시스템 제어 및 정밀농업 연구실

윤창호 올림